ADVANCED ENGINEERING MATERIALS
www.aem-journal.com

Scanning Manufacturing Parameters Determining the Residual Stress State in LPBF IN718 Small Parts

Itziar Serrano-Munoz, Alexander Ulbricht, Tobias Fritsch, Tatiana Mishurova, Arne Kromm, Michael Hofmann, Robert C. Wimpory, Alexander Evans, and Giovanni Bruno*

The influence of scan strategy on the residual stress (RS) state of an as-built IN718 alloy produced by means of laser powder bed fusion (LPBF) is investigated. Two scan vector rotations (90°-alternation and 67°-rotation), each produced following two different scan vector lengths (long and short), are used to manufacture four rectangular prisms. Neutron diffraction (ND) and laboratory X-ray diffraction (XRD) techniques are used to map the bulk and surface RS state, respectively. The distortion induced upon removal from the baseplate is measured via profilometry. XRD measurements show that the two long scan vector strategies lead to higher RS when compared with the equivalent short scan vector strategies. Also, the 67°-rotation strategies generate lower RS than their 90°-alternation counterparts. Due to the lack of reliable stress-free d_0 references, the ND results are analyzed using von Mises stress. In general, ND results show significant RS spatial non-uniformity. A comparison between ND and distortion results indicates that the RS component parallel to the building direction (*Z*-axis) has a predominant role in the *Z*-displacement. The use of a stress balance scheme allows to discuss the d_0 variability along the length of the specimens, as well as examine the absolute RS state.

1. Introduction

Metal-based additive manufacturing (AM) is a layer-by-layer production technique that has gathered considerable research focus in the past decade as it offers advantages unrivaled by conventional methods.[1–3] Chief among these advantages is the ability to produce lightweight complex-shaped parts with increased internal functionality (e.g., cooling channels), where assembly features can be significantly reduced or even eliminated. Particularly, laser powder bed fusion (LPBF) is an AM process where a high-energy laser beam selectively melts successive raked layers of powder under an inert gas atmosphere.

The use of AM Inconel 718 (IN718) is mainly driven by the aerospace and energy industries due to its good mechanical response and hot corrosion resistance at temperatures in the 650–700 °C range.[4] Moreover, its good weldability combined with high hardness and wear resistance (which leads to excessive tool wear when using machining subtractive methods) make IN718 particularly amenable to AM processing. However, despite the significant amount of research conducted on AM IN718 in recent years,[5] some relevant issues still require further research.[6] For instance, there is a limited understanding of the sensitivity of the microstructure and residual stress (RS) state to LPBF process parameters. For AM to mature to its full potential, attention has to be placed on the further understanding of the process–microstructure/RS relationship.

Direct application of a high-energy laser source leads to localized rapid solidification (in the order of 10^6 K s^{-1}) and cooling cycles. The resulting as-fabricated LPBF IN718 microstructure is nonequilibrium, multiscale, and highly heterogeneous. Broad grain size distributions as well as subgrain solidification cellular structures (their width can vary from 0.2 to 1 μm) are usually observed. These cellular structures are delineated by a high density of dislocations (the cell interiors are relatively dislocation free), as well as segregated alloying elements such as Nb and Mo.[7–11]

Literature works have also shown the potential of AM to tailor the material grain structure and texture, for instance, by altering the path that the heat source follows during selective melting (namely, the scan strategy).[12–16] This is because the

Dr. I. Serrano-Munoz, A. Ulbricht, Dr. T. Fritsch, Dr. T. Mishurova, Dr. A. Kromm, Dr. A. Evans, Prof. G. Bruno
8.5 Division
Bundesanstalt für Materialforschung und – prüfung (BAM)
Unter den Eichen 87, 12205 Berlin, Germany
E-mail: itziar.serrano-munoz@bam.de

Dr. M. Hofmann
Heinz Maier-Leibnitz Zentrum (MLZ)
Technische Universität München
Lichtenbergstr. 1, 85748 Garching, Germany

Dr. R. C. Wimpory
Department Microstructure and Residual Stress Analysis (CE-AME)
Helmholtz-Zentrum Berlin für Energie und Materialien
Hahn Meitner Platz 1, 14109 Berlin, Germany

Prof. G. Bruno
Institute of Physics and Astronomy
University of Potsdam
Karl-Liebknecht-Str.24-25, 14476 Potsdam, Germany

The ORCID identification number(s) for the author(s) of this article can be found under https://doi.org/10.1002/adem.202100158.

DOI: 10.1002/adem.202100158

solidification texture depends on competitive grain growth in one of the six <100> preferred growth directions in face-centered cubic alloys, as well as on the local heat flow direction.[17] Furthermore, different grain morphologies (i.e., columnar, where a grain can expand over several subsequent layers, or equiaxed) can be obtained by controlling the thermal gradient (G, $K\,m^{-1}$) and the solidification rate (R, $m\,s^{-1}$).[18]

Nevertheless, LPBF parts are highly vulnerable to RS, which, if uncontrolled, can lead to cracking, distortion, and/or undesired reduction of strength.[19–21] Such RSs are observed to have complex distributions and large magnitudes. The mechanisms responsible for the build-up of RS in LPBF are described to act at two levels: one involves the neighboring and directly laser-irradiated material, described by the temperature gradient model (TGM), and the other takes place between the latest added layer and the underlying solidified material; such a mechanism is taken into account by the cooled-down phase model.[22,23] At both levels, RS arises as the neighboring colder material prevents the free thermal expansion and contraction of the material being processed.

Analysis of RS in LPBF IN718 materials has been so far focused on long-range stresses (type I) that equilibrate over macroscopic dimensions (i.e., the scale of the part).[24] It is mainly observed that RS tends to be of tensile nature at the free surfaces of the part and compressive in the bulk.[25–27] Among the RS mitigation strategies that have been approached, tailoring the scan strategy has proven to be an effective solution, as it is reported that scanning with shorter scan vectors reduces the temperature gradient along the vector.[22,28–30] Furthermore, interlayer rotation of the scanning direction is reported to also induce lower RS magnitudes, as well as more uniform distributions of stresses.[23,28,30,31] The 67°-rotation is particularly interesting because in this case the scanning direction does not repeat for the maximum number of layers. Moreover, the 67°-rotation scan leads to an improved surface roughness quality.[32]

Between the diverse techniques to determine RS, nondestructive diffraction methods offer evident advantages and allow the study of postprocess effects such as the removal from the baseplate or heat treatments (HTs).[26,33,34] Nevertheless, the heterogeneity, lack of repeatability, and texture inherent to AM materials require a careful use of diffraction methods and a critical revision of the protocols in use for conventional materials (microstructures). For example, it has been observed that the elastic diffraction constants (DEC, which relates the measured lattice spacing to the macroscopic stress state) calculated by the Reuβ model (as opposed to the conventionally used Kröner model) are more suited for the RS analysis of textured LPBF IN718 microstructures.[35,36] This counterintuitive result has a very practical impact, as the correct determination of the bulk RS state is also necessary in the validation of computational models of the AM process. Further, the choice of the unstressed reference lattice parameter, d_0, has proven to be of paramount importance (as for any material), but even more challenging for AM materials.[37–39]

The main objective of the current work is to investigate the differences in RS state induced by changes in the LPBF scanning parameters: two scan vector rotations, each of them applied with two different scan vector lengths, are studied. The microstructural differences are examined using electron backscatter diffraction (EBSD). RS analysis is conducted by means of laboratory X-ray diffraction (XRD) and neutron diffraction (ND). We also study the effect of sample removal from baseplate on the RS state and part distortion. Finally, we discuss the use of powders and analytical conditions (i.e., stress balance) for the determination of the unstressed reference (d_0), the mechanisms involved in part distortion, as well as the main differences between the investigated scanning strategies.

2. Experimental Section

2.1. Manufacturing and Microstructure

The specimens were manufactured by Siemens AG, Power and Gas Division, Berlin, Germany, using an EOS M290 machine under an argon atmosphere. Prealloyed IN718 powders were used entirely in a virgin (not recycled) condition and the powder layer thickness was 40 μm. **Figure 1** shows the scanning patterns of 90°-alternation and 67°-rotation strategies (labeled as XY-scan and Rot-scan, respectively) applied using the so-called short (S) and long (L) scan vectors. The use of the short scan vector led to a strip width (SW, also known as hatch length) of $L/10$ (the parameter L indicates the X-dimension on the specimens), whereas the SW offset between successive layers was $L/20$. The use of the long scan vector led to an SW of $3\,L/4$, with an SW offset of $L/2$. According to the scan vector rotation and scan vector length, the four specimens being investigated were termed SXY-scan, SRot-scan, LXY-scan, and LRot-scan. The building direction (BD) was always parallel to the Z-axis. The top surface of all specimens underwent an up-skin process (corresponding to the last three layers, ≈120 μm), where the volumetric energy density was 4% lower than that applied to the rest of the specimen. The short and long scan vector specimens were produced in different build jobs. The specimens have the same orientation with respect to the recoater and the inert gas flow, being aligned at different positions along the Y-axis of the baseplate. The location of the SXY-scan specimen in the build chamber was identical to that of the LXY-scan specimen, and the same applies to the two Rot-scan specimens. The other process parameters are proprietary to Siemens and cannot be disclosed. The nominal yield strength in the as-built condition (as provided by the manufacturer) was $\sigma_{y\|BD} \approx 630$ MPa when parallel to BD and $\sigma_{y\perp BD} \approx 800$ MPa for the direction perpendicular to BD, which is in agreement with results reported in the literature by other authors.[40,41]

The microscopy samples (MS) were extracted (using electrical discharge machining, EDM) from one end of the specimens and the location of the microscopy observations is shown in Figure 1e. This extraction was conducted while the specimens were still attached to the 36 mm-thick baseplate. It has been reported that this sectioning does not significantly affect the RS state at the other end of the specimen.[42] Microstructural characterization of the specimens was conducted using a LEO 1530VP field-emission (FE) scanning electron microscope (SEM) equipped with an EBSD detector (Bruker Nano e-Flash HD 5030). The SEM was operated at an acceleration voltage and beam current of 20 kV and 7 nA, respectively. Sample preparation consisted of standard metallographic grinding and

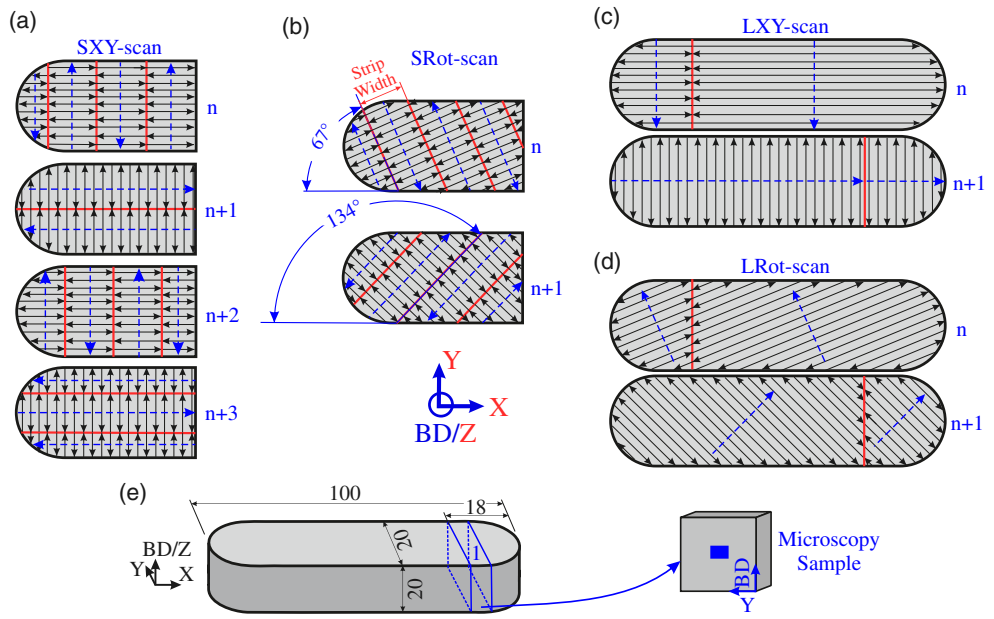

Figure 1. Schematic illustration of the scan strategies used in the manufacturing of a) the short scan vector at alternating *X*- and *Y*-directions (SXY-scan specimen), b) the short scan vector at 67°-rotation (SRot-scan specimen), c) the long scan vector at alternating *X*- and *Y*-directions (LXY-scan specimen), and d) the long scan vector at 67°-rotation (LRot-scan specimen). The red lines indicate the location and width of the hatching stripes, the black arrows indicate the rastering direction, and the blue arrows indicate the direction of advancement of the rastering. e) Schematic illustration of the geometry of the specimens (units in millimeters) showing the location of extraction of the MS, as well as the location of the SEM−EBSD observations (left).

polishing. The final polishing was conducted using 0.02 µm colloidal silica suspension.

The open-source MTEX toolbox (version mtex-5.2.8[43]) installed in MATLAB was used for EBSD data analysis. The step size of the EBSD maps was 4.7 µm. Two criteria were established for the quantitative analysis of the grains: 1) the misorientation between neighboring grains needed to be greater than 5; and 2) each grain needed to contain at least 2 data points. The texture intensity is described by the texture index, which becomes unity for isotropic material; consequently, anisotropic materials have an index higher than one.[44]

The four specimens were released from the baseplate by means of EDM. To remove the influence of the EDM processing (known to induce high tensile RS[22]) in the subjacent material and reliably conduct XRD analysis, the bottom surfaces of the two long scan vector specimens were ground with abrasive SiC papers down to P1200 grit (see **Figure 2**b). Subsequently, three bands (≈10 mm × 20 mm) at the bottom surface corresponding to the locations of CS1, CS2, and CS3 were electropolished using a Struers LectroPol-5 machine containing A2 electrolyte and operated at 34 V for 10 s. A total thickness of ≈100 µm was grounded/polished from the bottom surface, which was considered small enough (when compared with the 20 mm height) for the material removal to have a negligible effect on the bulk RS state.

2.2. Laboratory X-ray Angular Dispersive Diffraction (XRD)

The surface RS analysis was conducted using a Xstress G3 diffractometer (StressTech, Vaajakoski, Finland). This instrument worked in angular-dispersive XRD mode and consisted of a movable arm that carries an X-ray source and two position sensitive detectors, which rotate around a stationary specimen. A collimator aperture of 2 mm in diameter was used in front of a MnK_α radiation source. The exposure time for each data acquisition was 5 s. The penetration depth of this laboratory source was estimated to be ≈5 µm in Ni. The Ni-311 reflection ($2\theta = 156°$) was measured and the $\sin^2\psi$ method was used[45,46] for RS calculation. The movable arm was titled around an angular range from $\psi = -45°$ to $\psi = 45°$ for a total of evenly distributed 19 steps. The acquired data was processed with the software Xtronic, where the Pearson VII function was used for the peak fitting and a parabolic function was used for the background fitting. The diffraction elastic constants for Ni-311 reflection were calculated by the Reuβ model and are shown in **Table 1**. The explanation for the use of the Reuβ model can be found in other studies.[35,36] The occurrence of shear stresses (measured only at some reference points) was observed to be negligible.[15] As advised in the ISO standard 21432, the Ni-311 reflection was chosen based on it exhibiting low intergranular stress accumulation.[47,48]

Under the assumption of a biaxial stress state, any in-plane RS component can be obtained from the linear regression of the $\sin^2\psi$ versus lattice spacing relation. This calculation was made according to the standard DIN EN 15305:2009-01.[49] Note that the up-skin processing generated high surface quality at the uppermost surfaces, and so, it was considered that the XRD measurements on these surfaces were not affected by the relaxing effect of surface roughness, as is the case in the lateral surfaces.[35]

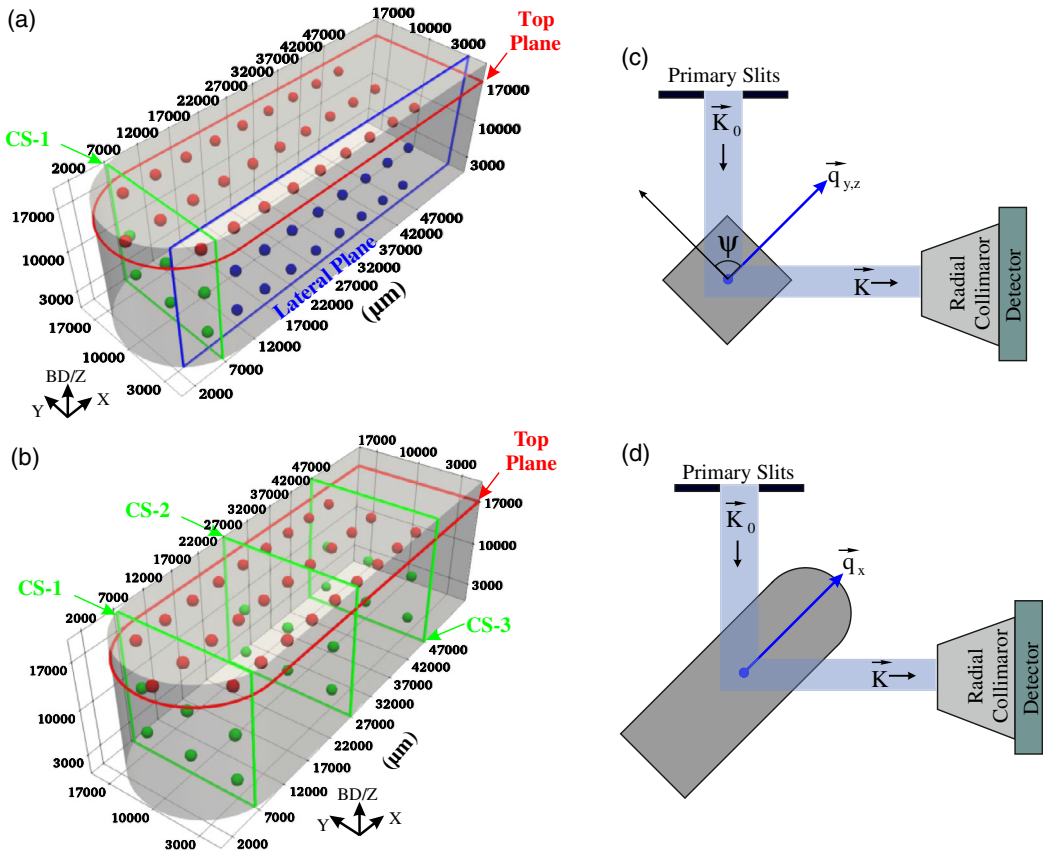

Figure 2. a) Location of the measurement points in the specimens investigated at E3 instrument. b) Location of the measurement points in the specimens investigated at STRESS-SPEC instrument. Schematic illustration of the instrument set-up at STRESS-SPEC, showing the specimens positioning for the measurement of c) the *Y* and *Z* components and d) the *X* component.

Table 1. RS evaluation parameters corresponding to the 311 reflection of the Ni single crystal and calculated using the Reuβ model.

Young's modulus $E^{\{311\}}$	178 GPa
Poisson's ratio $\nu^{\{311\}}$	0.34
Diffraction elastic constant $-S_1^{\{311\}}$	1.92×10^{-6} MPa^{-1}
Diffraction elastic constant $1/2S_2^{\{311\}}$	7.56×10^{-6} MPa^{-1}

2.3. Neutron Diffraction (ND)

While XRD is confined to the surface and near-surface region of a specimen, the high penetration depth of neutrons into matter (e.g., 20 mm into steel) allows the lattice spacing within the interior of parts to be measured.[50] The short scan vector specimens were investigated in the E3 beamline at BER-II reactor (Helmholtz Zentrum Berlin, Germany).[51] To comply with the weight limitation of the beamline translator stage, the specimens' baseplates were thinned using EDM (down to 6 mm). These two specimens were subsequently analyzed after complete removal from the baseplate (hereafter referred to as released [Re] condition). This beamline operated with a monochromatic neutron beam of $\lambda = 1.476$ Å wavelength, which led to $2\theta_{311} = 86.3$. The acquisition times varied between 5 and 90 min, depending on the measurement direction and location (Figure 2a). The gage volume was defined by setting the primary slits at 3 mm × 3 mm; the secondary collimator had a fixed focus width of 2 mm.

The long scan vector specimens were investigated only in the Re condition using the STRESS-SPEC instrument at FRM-II reactor (Heinz Maier-Leibnitz Zentrum, MLZ, Germany).[52] The monochromatic neutron beam was set at $\lambda = 1.550$ Å wavelength for the measurements to be carried out with a scattering angle of $2\theta_{311} \approx 90$. The intense neutron flux provided by FRM-II allowed the investigation of deeper locations (Figure 2b) and reduced the acquisition times, which varied between 2 and 25 min. The gage volume was defined by setting the primary slits at 2 mm × 2 mm; the secondary collimator had a focus width of 2 mm.

As no steep stress gradients were expected in the probed locations, the use of different gage volume sizes was assumed not to undermine the comparison of the calculated RS values. The average lattice spacing within the gauge volume was calculated by integrating the measured 2D diffraction data into a 1D pattern and fitting the resulting peak with a Gaussian function on the flat/fitted background. This calculation was carried out using the custom program StressTexCalculator.[53] For each measurement point, the strains (ε) were calculated according to

$$\varepsilon = \frac{d_{311} - d_0^{311}}{d_0^{311}} = \frac{\sin\theta_0^{311}}{\sin\theta_{311}} - 1 \quad (1)$$

Assuming isotropic elastic properties, the stresses in the principal geometric axes *X, Y, Z* were calculated via Hooke's law using the following equation.

$$\sigma_{X,Y,Z} = \frac{E^{311}}{(1+\nu^{311})(1-2\nu^{311})} \times \left[\left(1-\nu^{311}\right)\varepsilon_{X,Y,Z} + \nu^{311}(\varepsilon_{Y,Z,X} + \varepsilon_{Z,X,Y})\right] \quad (2)$$

Von Mises (VM) stresses were calculated according to

$$\sigma_{VM} = \sqrt{\frac{1}{2}[(\sigma_X - \sigma_Y)^2 + (\sigma_Y - \sigma_Z)^2 + (\sigma_Z - \sigma_X)^2]} \quad (3)$$

For the case of planar stress (assumed for XRD analysis), the $\sigma_N = 0$ (i.e., the stress component perpendicular to the free surface). Note that distortions are not related to hydrostatic stresses and therefore will be compared with VM stresses.[54]

2.4. Determination of the Stress-Free Reference d_0

The determination of a reliable value of the stress-free lattice spacing is probably the most critical issue for RS analysis via ND. This is because small experimental errors in the d_0 determination can lead to significant variations in the calculated stress. For instance, a shift of 0.01 in d_0 value leads to a stress variation of ≈20 MPa in the case of the studied IN718 alloy.

In the present study, the d_0 lattice spacing was evaluated using raw powders (which were extracted from the batch used in the powder bed) and mechanical filings (extracted from the as-build specimens). Note that the raw powders underwent a different thermal history during the atomization process, which is believed to induce a shift in the diffraction peak due to a different chemical segregation.[25] Thus, the raw powders were thought to be used only as a stable reference for comparison between different beamtimes and neutron instruments. Also, to remove any remaining short-range RS (i.e., Type II/III) in the mechanical filings, a HT at 450 °C for 4 h was applied under a middle-to-high vacuum level (≈ 10^{-3} mbar). It was assumed that this low-temperature HT (compared with the 900–1000 °C HT generally used for parts) would suffice to reduce the remaining short-range RS without significantly altering the chemical composition of the mechanical filings references.[55]

Imposing a stress balance scheme over a cross section of the sample allows the determination of d_0 without having to measure a reference sample, under the assumption that the d_0 value is constant across the section.[56] This procedure requires the RS field across the entire cross section to be determined ($\int_A \sigma_n dA = 0$). As only discrete measurements were taken in the cross section, the integral can be replaced by summations, and the stress balance is given by

$$\sum \sigma_\perp \Delta S|_S = 0 \quad (4)$$

where *S* is the area of each measurement point. A custom Python routine was developed; the XRD and ND values were interpolated over a 2 mm × 2 mm grid (equal to the gage volume of the STRESS-SPEC measurements). The surface RS determined by XRD were retained as input values, whereas the reference d_0 of the ND measurement was iteratively varied until the stress balance condition (Equation (4)) was fulfilled.

2.5. Distortion Measurements

The distortion characterization following the baseplate removal was conducted by measuring the *Z*-displacement of the top surface. A white-light (diode emitting between 400 and 3400 nm) profilometer (an FRT MicroProf device with an FRT CWL sensor) was used. The area investigated was 19 mm × 60 mm with a step size of 20 µm and a scanning speed of 794 µm s^{-1}. After removal from the baseplate, the acquired data needed processing for the correction of parallelism defects (i.e., after EDM, bottom surfaces were not perfectly parallel to top surfaces).

3. Results

3.1. Grain Structure and Texture

The complexity of the grain structures resulting from LPBF processing is shown in **Figure 3**. The primary difference between the XY- and Rot-scan strategies is the ability of the former to create columnar grains (Figure 3a,c), whereas the latter produces elongated grains with the mayor axis predominantly parallel to the BD (Figure 3b,d). Note that the elongated grains also undergo epitaxial growth but the higher variation of the heat flow direction during the 67°-rotation processing allows for a higher number of grains to form during solidification. The (100) pole figures show a mild cube texture corresponding to the predominance of red-colored grains in the grain orientation map for the YZ plane of the SXY-scan sample (Figure 3a). This sample exhibits the highest texture index (3.1) of all the specimens shown in Figure 3. A smaller grain size and stronger variation of the orientation between neighboring columnar grains in the LXY-scan specimen (Figure 3c) reduces the texture index to 2.1. In both XY samples, the fine array of grains occurring at the center of melt pools[13,14] have a <001> preferential orientation, whereas the columnar grains do not show any significant orientation preference. In comparison with the XY-scan strategies, the two Rot-scan samples exhibit both similar grain structures and texture intensities (≈1.1).

3.2. Surface RS

As shown in **Figure 4**a, each specimen was investigated in three conditions: 1) the as-built condition, corresponding to the state with the original baseplate thickness (36 mm), 2) the thin baseplate (TB) condition, where the baseplate was EDM thinned, and 3) the Re condition, where the baseplate was completely removed (EDM). The measurement points were restricted to one-half of each specimen (50 mm) and located along a central line.

Regardless of the stress component (see Figure 4b–g), the RS values are always the highest in the long scan vector specimens for the as-built condition. Moreover, the LXY-scan specimen shows slightly (≈50 MPa) higher RS compared with the LRot-scan specimen. In addition, the SXY-scan strategy yields higher RS than the SRot-scan specimen, by ≈30 MPa. For σ_X

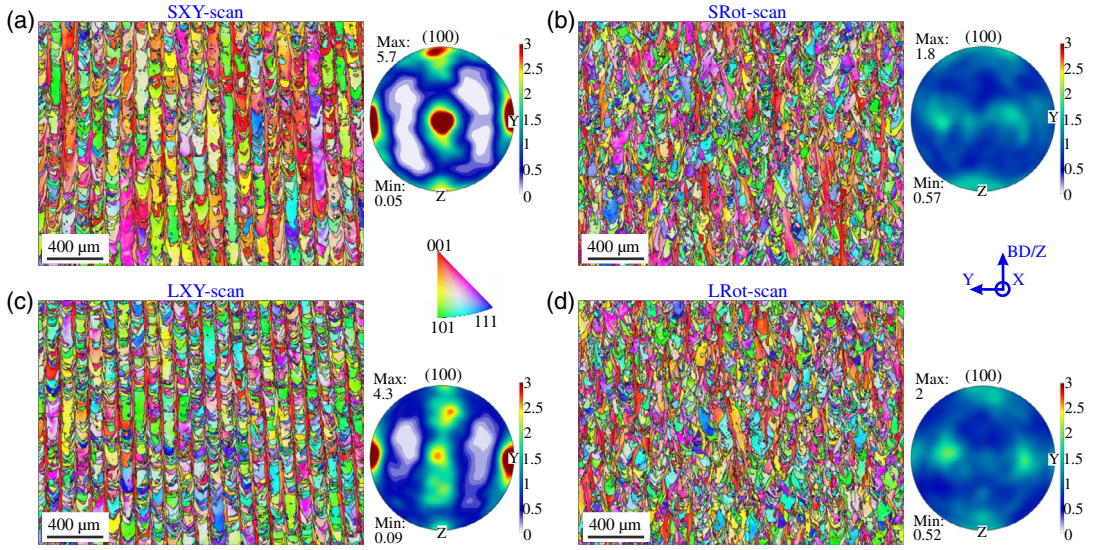

Figure 3. EBSD orientation maps with inverse pole figure (IPF) coloring in the Z/BD-direction and corresponding (100) pole figures for a) the SXY-scan specimen b) the SRot-scan specimen, c) the LXY-scan specimen, and d) the LRot-scan specimen.

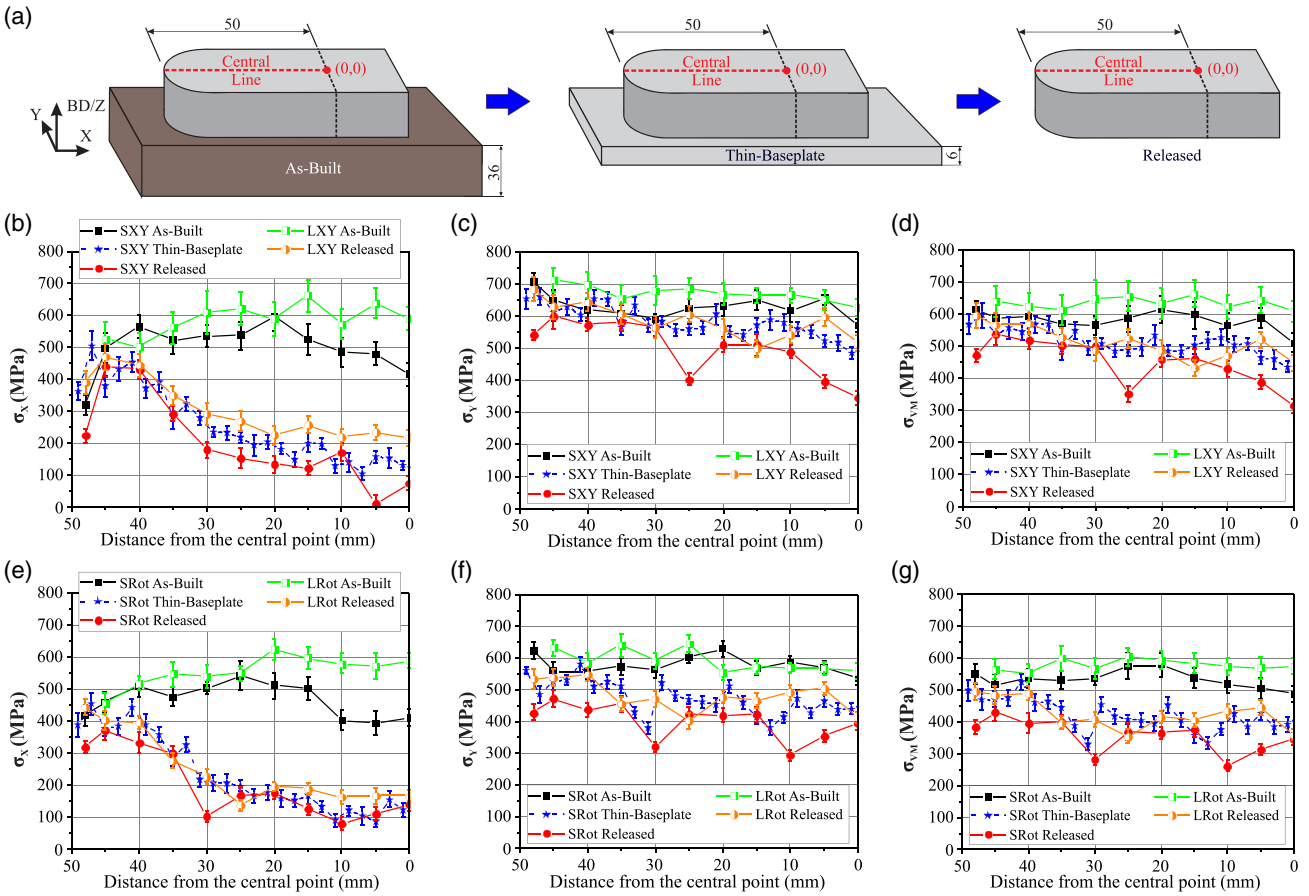

Figure 4. a) Schematic illustration of the location of the XRD measurement points and of the investigated conditions, labeled as as-built (left of the image), TB (center, only for the short scan vector specimens), and Re (right). Plots of the RS analysis conducted on the XY-scan specimens for b) the *X* component, c) the *Y* component, and d) the VM component. Plots of the RS analysis conducted on the Rot-scan specimens for e) the *X* component, f) the *Y* component, and g) the VM component. The data corresponding to the short scan vector specimens are replotted from the study by Serrano-Munoz et al.[35]

(Figure 4b,e), both the long and the short scan vector specimens exhibit similar values from the 50 to 40 mm region. In the region between 40 mm distance and the specimen center, the RS values diverge until the highest difference (≈150 MPa) between XY- and Rot-scan specimens is observed at 0 mm (specimen center). For σ_Y (see Figure 4c,f), the stress difference between XY- and Rot-scan specimens is reduced when compared with σ_X. In this case, the RS values fluctuate between 550 and 700 MPa, which are about ≈50 MPa higher than those observed for σ_X.

The thinning of the baseplate induces a significant relaxation of σ_X for both the SXY- and SRot-scan specimens (Figure 4b,e). Interestingly, the 50−40 mm region (at the specimen tip) does not undergo any substantial relaxation. A steep reduction (≈200 MPa) is observed in the 40−30 mm region, whereas from the 30 to 0 mm region the RS values stabilize at 100−200 MPa. The total amount of relaxation in the 30−0 mm region is about 300 MPa. The corresponding RS relaxation is smaller for σ_Y (Figure 4c,f): about 50 MPa for the SXY-scan sample and about 150 MPa for the SRot-scan specimen. However, in the 50−40 mm region, the RS is barely relaxed.

The removal of the thinned baseplate marginally reduces the RS values of the SXY- and SRot-scan specimens in the *X*-direction. A greater reduction (about 50 MPa) is observed for the *Y*-direction component (Figure 4b,c,e,f). The Re condition of the LXY- and LRot-scan specimens systematically exhibits RS values higher than those of the SXY- and SRot-scan specimens for both σ_X and σ_Y. Moreover, the differences between short and long scanning are slightly higher for the XY-scan strategies.

For all the investigated conditions, the von Mises equivalent RS (σ_{VM}, Figure 4d,g) shows the same tendencies as those observed in σ_Y, although the difference between the as-built and Re conditions is larger. Note that some of the RS distributions in Figure 4 exhibit undulations in the Re condition at 25 mm of the SXY-scan specimen and at 30 and 10 mm of the SRot-scan specimen. These undulations correspond to the location of borders/grooves between adjacent hatching stripes (more details on this matter are given in the study by Serrano-Muoz et al.[35]).

3.3. Bulk RS

3.3.1. Absolute RS through Stress Balance

To apply stress balance conditions and complete the stress maps, XRD measurements were carried out over the perimeter of the three cross sections of the LXY- and LRot-scan specimens (see **Figure 5**a). The stress balance results of the CS2 (Figure 2b) of both LXY- and LRot-scans are shown in Figure 5b,c as an example. This stress balance scheme yields a $2\theta_{SB}$ value that is subsequently used for the calculation of the absolute RS components. As the $2\theta_{SB}$ values obtained for each cross section are similar, the average of the six calculated $2\theta_{SB}$ is used in the determination of the absolute RS.

Interestingly, the interpolation results indicate that the maximum of the compressive center is located at a slightly higher position ($Z \approx 12$ mm) in the LYX-scan specimen than in the LRot-scan one ($Z \approx 10$ mm). The upward shift of the compressive center in the LYX-scan specimen leads to steeper RS gradients being formed from 20 mm down to 17 mm height (Figure 5b) when compared with those of the LRot-scan specimen (Figure 5c). Consequently, the absolute RS maps in the top plane (3 mm below the uppermost surface, see Figure 2b) show lower values in the LXY-scan specimen (**Figure 6**). Nevertheless, the RS distributions are similar in the two specimens. In Figure 6, the highest tensile (or highest compressive) values are systematically observed at the central line ($Y = 10$ mm). Also, an asymmetry with respect to the *X*-axis is observed, mainly localized in the $X = 7$–20 mm region.

The RS cross-section maps for σ_Z are shown in **Figure 7**. Significant asymmetry with respect to the *Z*-axis is observed in the three cross sections of the two samples. The central values at CS1 are considerably higher (by ≈200 MPa) than those observed at CS2 and CR3. In addition, the center of LXY Re CS2 exhibits lower compressive stress (a difference of ≈50 MPa) than the center of LRot Re CS2 (Figure 7c,d). This observation is reversed at CS3: the center of LRot Re CS3 exhibits lower compressive stress (≈50 MPa) than the center of LXY Re CS3 (Figure 7e,f). Other than the above differences, all six maps look similar: no significant qualitative/distribution differences are observed along the *X*-axis. Moreover, the other two principal components (σ_X and σ_Y) show similar features to the ones observed in Figure 7. For further comparison, the σ_X and σ_Y RS maps are given as Supporting information.

3.3.2. Von Mises Stresses

The stress relaxation from the TB to the Re conditions of the SXY- and SRot-scan specimens is shown in **Figure 8**, for the case of the top plane. In the TB condition, both specimens display a

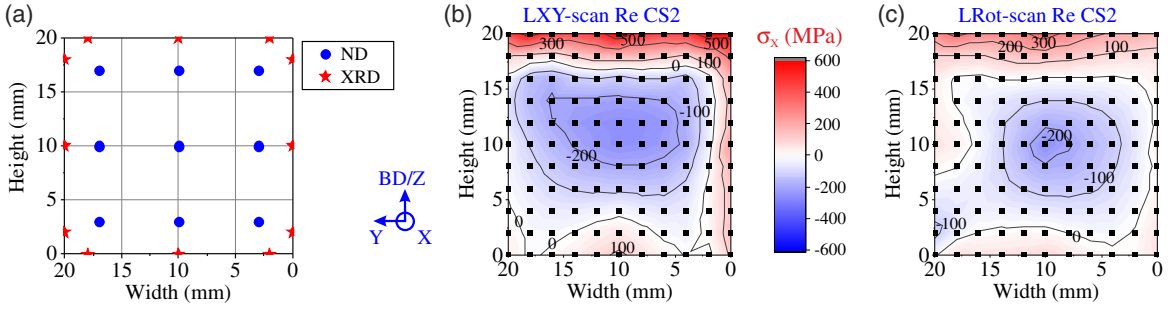

Figure 5. a) Graph showing the location of the XRD surface points and the ND bulk points. σ_X RS maps in the Re condition in CS2 resulting from the stress balance calculation for b) the LXY-scan and c) LRot-scan specimens. The black squares indicate the location of the interpolation points.

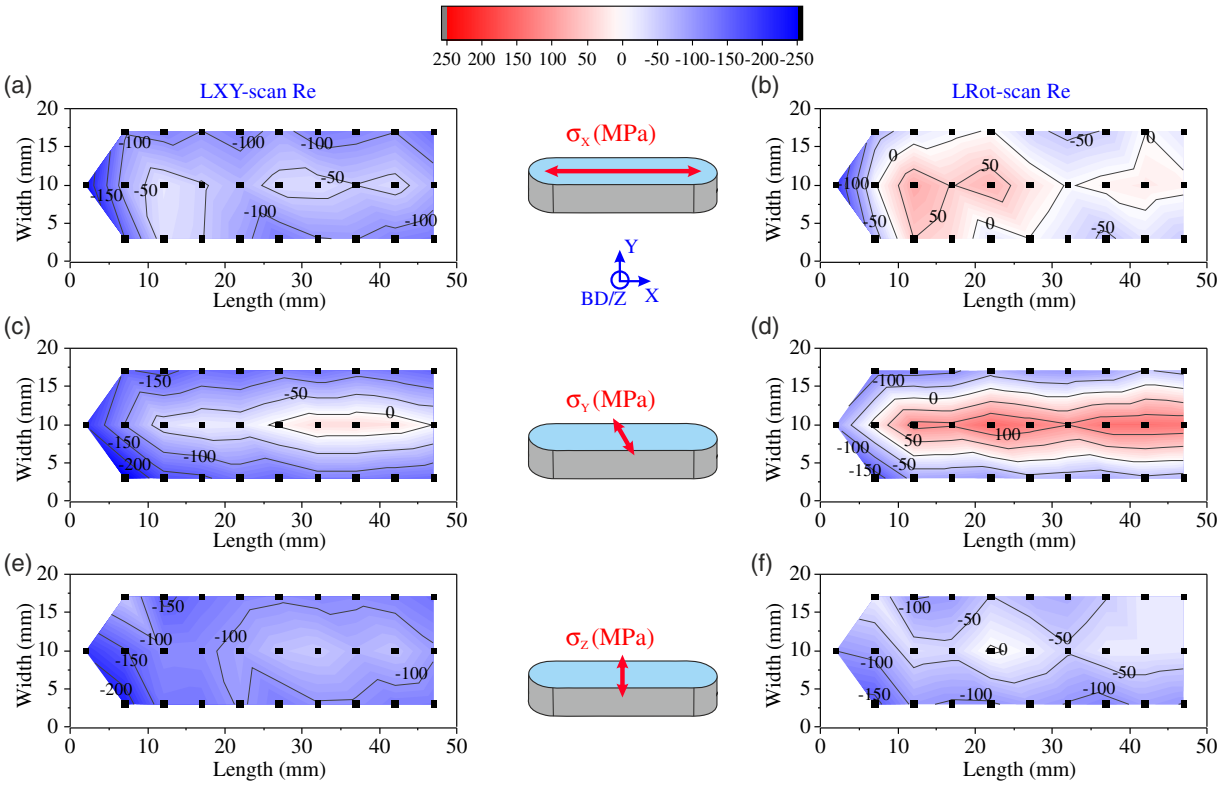

Figure 6. Absolute RS maps of the top plane in the Re condition obtained using $2\theta_{SB}$ and showing σ_X results for a) the LXY-scan and b) the LRot-scan specimens; σ_Y results for c) the LXY-scan and d) the LRot-scan specimens; σ_Z results for e) the LXY-scan and f) the LRot-scan specimens. The stress scale bar (in MPa) is given on top. The average error for all the points is ±40 MPa.

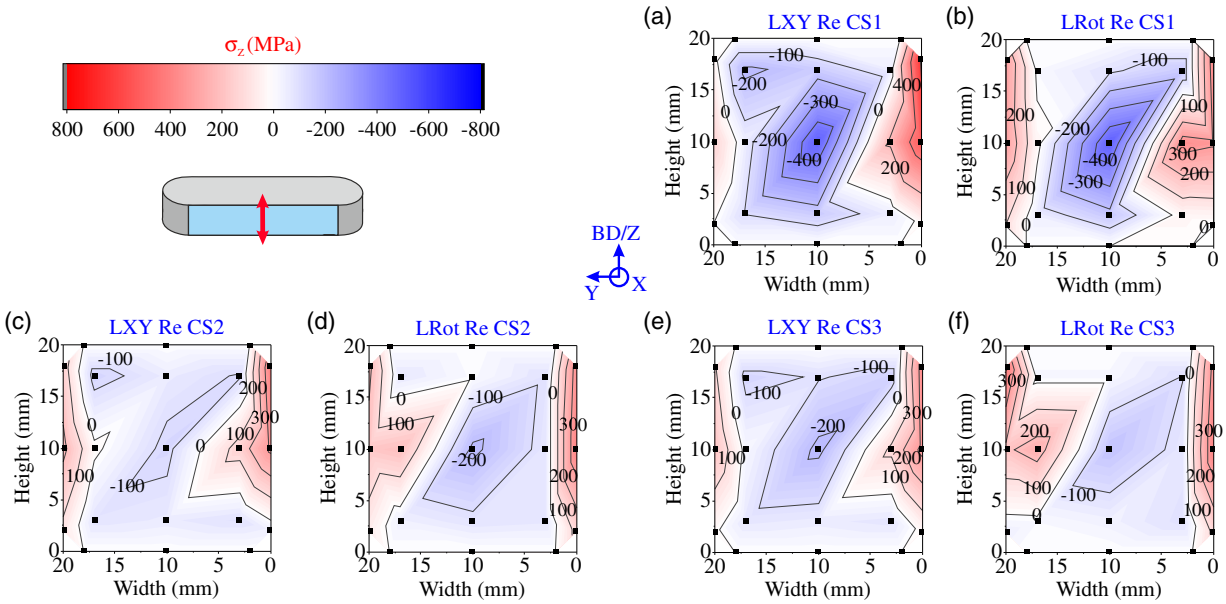

Figure 7. σ_Z maps in the Re condition obtained using $2\theta_{SB}$ and showing a) CS1 of the LXY-scan specimen, b) CS1 of the LRot-scan specimen, c) CS2 of the LXY-scan specimen, d) CS2 of the LRot-scan specimen, e) CS3 of the LXY-scan specimen, and f) CS3 of the LRot-scan specimen. Note that the XRD and ND data are combined. The average error for all the points is ±35 MPa.

central band along the *X*-axis where the highest values are observed. In this case (as opposed to Figure 6), the SXY-scan specimen shows slightly higher values that its SRot-scan counterpart. No significant relaxation is observed after removal of

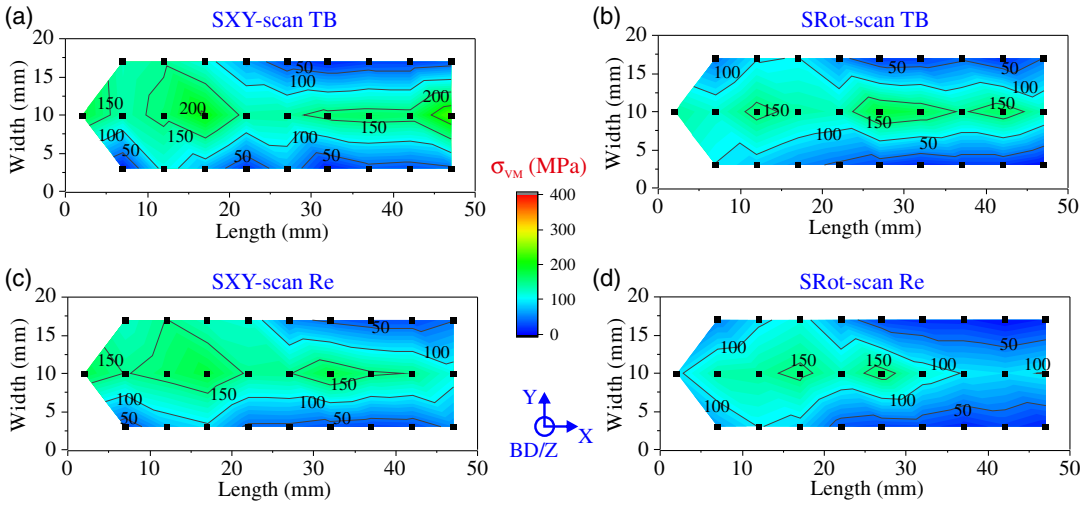

Figure 8. σ_{VM} maps of the top plane for a) the SXY-scan specimen in the TB condition, b) the SRot-scan specimen in the TB condition, c) the SXY-scan specimen in the Re condition, and d) the SRot-scan specimen in the Re condition. The average error for all the points is ±52 MPa.

the TB: the central band remains and most of the relaxation occurs in the $X = 35-47$ mm region in both specimens.

The VM RS maps of the lateral plane in the TB condition also exhibit a central band ($Z = 10$ mm), where the highest values occur (**Figure 9**a,b). The SRot-scan specimen exhibits the highest values, localized mainly in the $X = 42-17$ mm region. At the bottom, the SRot-scan strategy leads to slightly lower values. In both specimens, the lowest values are observed at the top line. The relaxation after baseplate removal is higher than in the top plane and leads to similar Re RS distributions between the two specimens (Figure 9c,d). The highest relaxations (>100 MPa) are observed at the bottom of the two specimens,

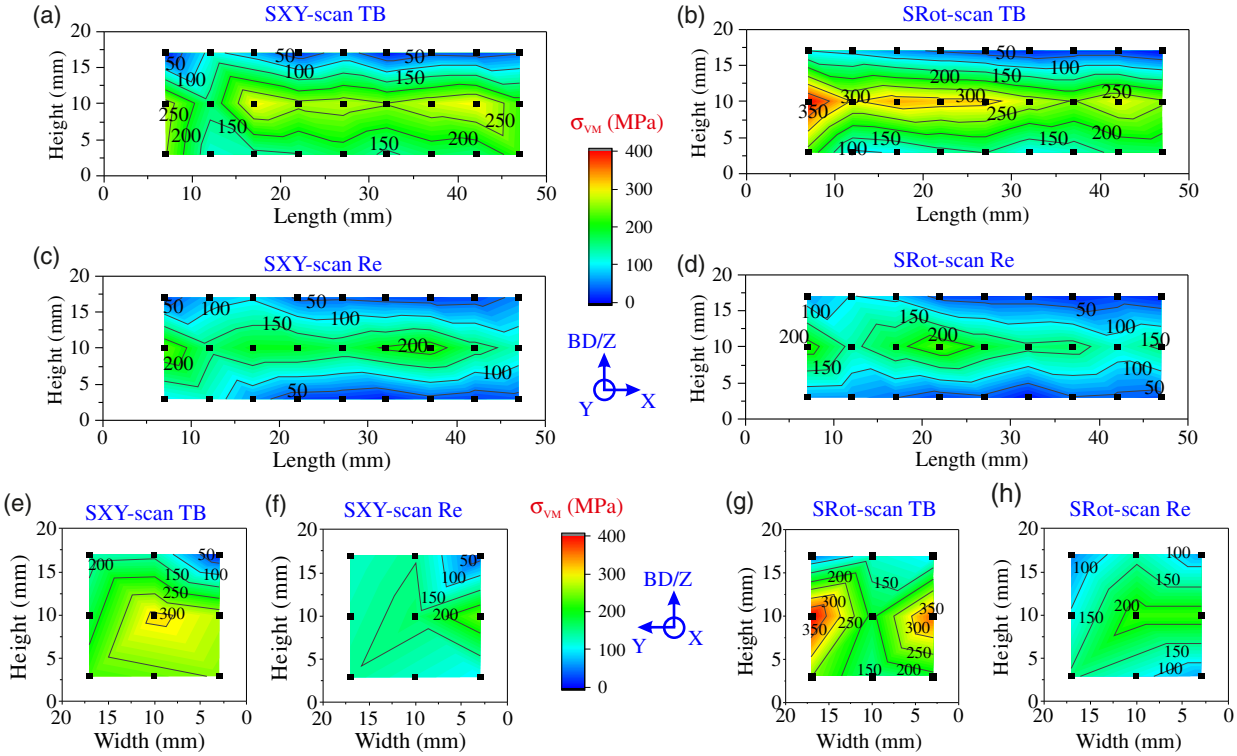

Figure 9. σ_{VM} maps of the lateral plane for a) the SXY-scan specimen in the TB condition, b) the SRot-scan specimen in the TB condition, c) the SXY-scan specimen in the Re condition, and d) the SRot-scan specimen in the Re condition. σ_{VM} maps of CS1 for e) the SXY-scan specimen in the TB condition, f) the SXY-scan specimen in the Re condition, g) the SRot-scan specimen in the TB condition, and h) the SRot-scan specimen in the Re condition. The average error for all the points is ±55 MPa.

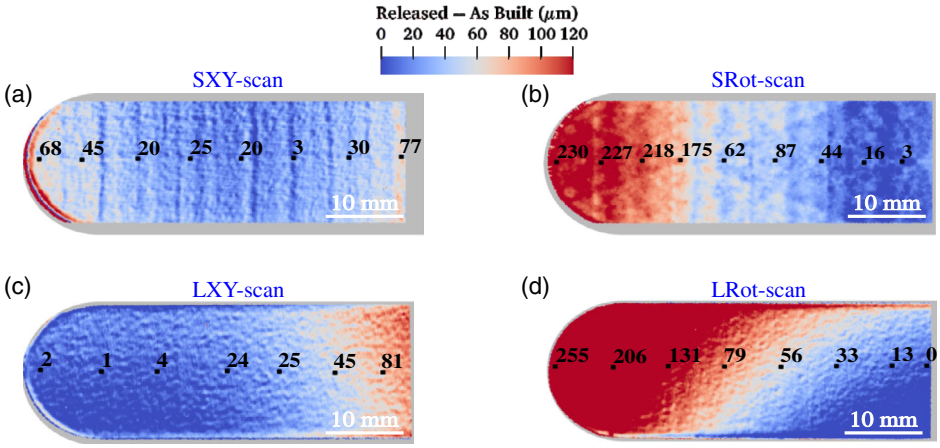

Figure 10. *Z*-displacement distortion maps of the difference between the Re and as-built conditions for a) the SXY-scan specimen, b) the SRot-scan specimen, c) the LXY-scan specimen, and d) the LRot-scan specimen.

and the highest values are still observed in the middle ($Z = 10$ mm).

In the cross sections, the highest values occur at the middle height ($Z = 10$ mm) of the specimens (Figure 9e,g). Again, the RS distribution becomes similar after baseplate removal (Figure 9f,h). Contrary to the RS distributions typically observed in cross sections (such as the one shown in Figure 9e), the SRot-scan specimen shows localization of the highest values at the lateral sides instead of at the center (Figure 9 g).

3.4. Z-Axis Distortion upon Baseplate Removal

Figure 10 shows that the main distortion differences are induced when changing from the XY-scan to the Rot-scan strategy. The two ends of the SYX-scan specimen show upward bending (along the *Z*-axis), whereas nearly zero *Z*-displacement is observed in the $X = 35$–25 mm region. In contrast, the LXY-scan specimen shows upward bending only in the right end. Some twisting around the X-axis is also observed. On the other hand, the two Rot-scan specimens exhibit upward bending only at the left side. The highest *Z*-displacement values correspond to the LRot-scan specimen. Moreover, this specimen exhibits a more noticeable twisting around the *X*-axis, when compared to the LXY-scan specimen.

4. Discussion

4.1. d_0 determination

As introduced in Section 2.4, the raw powders do not provide a reliable d_0 value.[25] When using the reference 2θ value obtained from raw powders in the as-received condition (see **Figure 11**) for the calculation of absolute RS, the values of the points in the top plane are similar to the XRD results measured at the uppermost surface (shown in Figure 4). Given that a strong RS gradient is expected to occur between the uppermost surface and 3 mm depth, it is considered that the raw powders renders an unreliable d_0 reference. In contrast, using the reference 2θ value of the

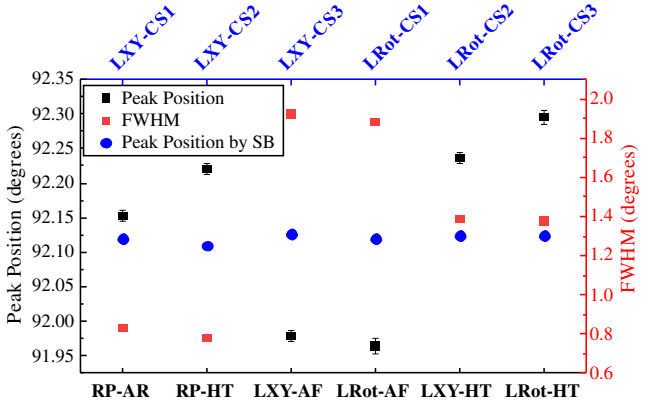

Figure 11. Plot of the diffraction peak position (right) and FWHM (left), against the type of powder being analyzed (bottom) where the labels correspond to raw powders (RP-AR [as-received] and RP-HT [heat treated]) and sample filings (LXY-AF [as-filed], LXY-HT, LRot-AF, and LRot-HT). The results shown at the top axis correspond to the $2\theta_{SB}$ values of each cross section calculated by stress balance (SB).

mechanical filings leads to compressive stress for all measured points, which also questions the reliability of mechanical filings. For the sake of brevity, only the results obtained at STRESS-SPEC beamline are shown in Figure 11, as those obtained at E3 beamline show similar tendencies.

The heat treatment (HT) has two effects in both the raw powders and the mechanical filings: it increases the 2θ values while reducing the full width at half maximum (FWHM) values. The 2θ shift is lower in the raw powders (0.075) than in the mechanical filings. Nonetheless, this shift observed after HT of the raw powders still induces a significant difference in the calculated values (equivalent to a $\approx 800\,\mu\varepsilon$ shift). Using any of the 2θ values obtained after HT leads to entirely tensile RS maps. The raw powders shift of the FWHM value is considered negligible when compared with those of the mechanical filings. This difference in FWHM indicates that a more significant plastic recovery takes place in the mechanical filings during the HT process.

In this context, the high accumulation of plastic strain is proposed as the principal factor leading to the biased 2θ reference values obtained using mechanical filings in the as-filed condition. As for the mechanism inducing the 2θ shift after HT on both the raw powders and mechanical filings, it is presumed that some compositional changes (i.e., elemental diffusion without any morphological change, e.g., precipitation of γ" phase) occur in the nonequilibrium γ-Ni matrix during the HT at 450 °C. Most likely, at this temperature the atoms in solid solution in the γ-Ni matrix would migrate to thermodynamically more stable zones such as cell walls and grain boundaries, presumably decreasing the solute-atom lattice distortion of the γ-Ni matrix (note that a shift to higher 2θ values indicates a decrease in the lattice spacing). Further, we do not exclude that some degree of oxidation could have occurred during the HT, possibly due to imperfect vacuum, also contributing to the peak shift observed in the powders and filings.

Given the limitations encountered when using mechanical filings, we consider that the imposition of stress balance conditions leads to a more reliable d_0 value. According to the stress balance calculation carried out at each cross section (blue dots in Figure 11), there should not be any significant compositional changes along the *X*-axis of the two specimens. Furthermore, this calculation predicts no significant d_0 variation between the two specimens. It has to be noted that several assumptions are made when applying stress balance conditions and their influence has to be considered in the evaluation of the absolute RS results (Section 3.3.1).

First, and as also argued in another study,[35] it is still to be determined if the difference in compositional and dislocation content between the dendritic cell interior and dendritic cell walls (where the elemental microsegregation and dislocation density is highest) could induce some triaxiality in the stress state at near-surface depths (≈45 μm)[59] (i.e., similar to that observed in composites[24]), which would invalidate the $\sigma_N = 0$ MPa assumption. Given that in the present study the depth probed by XRD is ≈5 μm, the stress component normal to the investigated surface is assumed to be zero, and so, the $\sin^2\psi$-method can be applied.

The stress balance condition also assumes that there are no d_0 compositional variation over the investigated cross section. In this regard, recent studies report that no significant d_0 variation occurs in LPBF IN718 alloy,[26,27] whereas a d_0 variation has been reported to occur in a laser-based directed-energy deposition IN625 wall, where the content of Cr decreases as the height of the BD increases.[57] This indicates that the d_0 variation depends on the process and/or material and cannot be generalized to all AM materials. Thus, based on the prior art,[26,27] it is considered that no compositional variation occurs over the investigated cross sections.

Finally, the stress balance calculation assumes a linear interpolation between the bulk and surface data. The tensile RS values should be highest at the very surface (corresponding to the XRD results). In the case of the investigated specimens, it was observed that the roughness occurring at the lateral surfaces relaxes the RS values measured at 5 μm depth,[35] and so, subsurface maxima are expected to occur at both lateral surfaces. We therefore consider that the presence of subsurface maxima underestimates the absolute RS values but not the general trends observed in Section 3.3.1.

4.2. Main Differences Induced by the Scan Strategy

As expected, the XRD results (Figure 4) show that the long scan vector strategies lead to higher RS magnitudes than their short scan vector counterparts due to the presence of larger thermal gradients.[23,28] Also, the XY-scan strategy induces higher RS values when compared with those resulting from the Rot-scan strategy, because the 67°-rotation would induce a better redistribution of the heat flux and internal stresses than the 90°-alternation, which repeats faster.[32] Apart from the differences in magnitudes, all samples exhibit similar RS distributions in the as-built condition, where the σ_Y values are generally higher (by ≈50 MPa) than the σ_X. Note that a longer scan vector does not always imply larger RS, as it has been observed in a LPBF Ti-6Al-4V material, where a shorter island scan strategy leads to larger RS.[60] Hence, and as also stated in the study by Ganeriwala et al.,[60] caution must be taken when generalizing the presented results beyond the current material and geometry.

The thinning of the baseplate induces significant σ_X relaxation (≈250−300 MPa), whereas the σ_Y relaxation is lower (≈100 MPa). Comparatively, the removal of the thinned baseplate induces low relaxation (≈50 MPa) of these two stress components. Furthermore σ_{VM} (Figure 4 d,g) exhibits similar relaxation for all specimens, whereas the distortion results (Figure 10) show differences in relaxation, mainly when changing the scanning strategy from XY-scan to Rot-scan. As further explained below, this lack of agreement between surface σ_{VM} (which does not take into account σ_Z) and distortion results can be explained if one considers that the $\sigma_{Z/\mathrm{BD}}$ exerts the highest influence on the *Z*-displacement.

The bulk σ_{VM} results show the same tendency at the top plane: the SRot-scan specimen has slightly lower values than the SXY-scan one in the TB condition and no significant differences are observed between the two specimens in the Re condition (Figure 8). However, the lateral plane and CS1 maps (Figure 9) indicate higher σ_{VM} occurring within the Rot-scan specimen in the case of the TB condition. And again, these maps show similar σ_{VM} distributions between the two specimens in the Re condition. Probably, the difference between the results observed in the top and lateral planes is induced by higher $\sigma_{\mathrm{BD}/Z}$ values occurring in the TB SRot-scan specimen. Higher $\sigma_{\mathrm{BD}/Z}$ values in the SRot-scan specimen than in the SXY-scan one were also reported in the study by Serrano-Munoz et al.[35]

The differences in the $\sigma_{\mathrm{BD}/Z}$ values and distribution suggest a variation in the interaction mechanism between the successive layers depending on the scanning strategy.[15,32] The XY-scan strategy would induce higher RS in the XY-plane, whereas the Rot-scan strategy would lead to higher RS along the BD. Hence, the distortion maps (Figure 10) would reflect these differences in $\sigma_{\mathrm{BD}/Z}$, with the Rot-scan strategy exhibiting higher *Z*-displacement at the left end of the two specimens.

Finally, it is also observed that both XY- and Rot-scan strategies lead to significant nonuniform (asymmetric) VM RS fields, which are inherently generated by the process.[28] This nonuniformity is difficult to predict uniquely using XRD methods. Moreover, increasing the length of the scan vector further increases the nonuniformity of the RS distribution. Supposedly, this increase in nonuniformity would lead to the

twist around the *X*-axis observed in the distortion maps (Figure 10c,d).

5. Conclusion

A comprehensive investigation of the variations in RS state resulting from changes in the laser scanning pattern has been conducted. EBSD analyses show the primary differences in grain structure and texture. XRD on the uppermost surface allows to quantify the differences in RS state and monitor the effect of the thinning and removal from baseplate. ND gives insight into the distribution of the bulk RS fields. Finally, distortion maps allow to examine the differences in *Z*-displacement between specimens. As a result, the following conclusions can be drawn:

1) The two XY-scan strategies produce columnar grains, whereas the Rot-scan strategies lead to elongated grains (i.e., epitaxially grown grains with lower aspect ratio and increased shape complexity). The main axis of these two types of grains is predominantly parallel to the BD. The LXY-scan strategy tends to reduce the grains size and texture intensity when compared with the SXY-scan strategy. The Rot-scan samples exhibit similar grain structure and texture. 2) XRD results show, on average, higher RS magnitudes in the as-built specimens produced using the long scan vector strategies. The SRot-scan strategy leads to the lowest RS values of all investigated specimens. After total removal from the baseplate, all specimens undergo significant σ_X relaxation ($\approx$250 MPa). The σ_Y relaxation is less significant (50−100 MPa). 3) Neither the raw powders nor the mechanical filings give a reliable value of the d_0 unstressed reference. 4) σ_{VM} maps show an increased nonuniformity when applying long scan vectors. 5) Different distortion distributions are observed depending on the scan strategy. Upward bending along the *Z*-axis is observed in all specimens, although the long scan vector specimens also exhibit a certain degree of twisting along the *X*-axis. 6) The d_0 determination by imposition of stress balance conditions is done with the main assumption of a unique d_0 value (i.e., no spatial chemical variation over the cross section). This calculation predicts similar d_0 values along the length of the specimens. The d_0 value would also be similar between the SLX- and SRot-scan specimens. 7) The differences in the distortion behavior are mainly correlated with the effect that the scanning strategies have on the build-up of RS along the BD.

Supporting Information

Supporting Information is available from the Wiley Online Library or from the author.

Acknowledgements

René Hesse is acknowledged for assisting in the distortion measurements. Romeo Saliwan-Neumann and Naresh Nadammal are acknowledged for their contribution to the microstructural characterization. Gratitude is also expressed to Mareike Kirstein for conducting electropolishing. Finally, the authors would like to thank Siemens AG Power and Gas Division, Berlin, Germany, for producing and supplying the investigated specimens.

Open access funding enabled and organized by Projekt DEAL.

Conflict of Interest

The authors declare no conflict of interest.

Data Availability Statement

Data available on request from the authors.

Keywords

AM as-built IN718 alloy, distortion upon baseplate removal, laser powder bed fusion technique, neutron diffraction, residual stress state, influence of scan strategy, stress balance conditions

Received: February 5, 2021
Revised: March 24, 2021
Published online:

[1] D. Herzog, V. Seyda, E. Wycisk, C. Emmelmann, *Acta Mater.* **2016**, *117*, 371.
[2] W. J. Sames, F. A. List, S. Pannala, R. R. Dehoff, S. S. Babu, *Int. Mater. Rev.* **2016**, *61*, 315.
[3] T. DebRoy, H. L. Wei, J. S. Zuback, T. Mukherjee, J. W. Elmer, J. O. Milewski, A. M. Beese, A. Wilson-Heid, A. De, W. Zhang, *Prog. Mater Sci.* **2018**, *92*, 112.
[4] R. C. Reed, *The Superalloys Fundamentals and Applications*, Cambridge University Press, Cambridge **2006**.
[5] E. Hosseini, V. A. Popovich, *Addit. Manuf.* **2019**, *30*, 100877.
[6] T. DebRoy, T. Mukherjee, J. O. Milewski, J. W. Elmer, B. Ribic, J. J. Blecher, W. Zhang, *Nat. Mater.* **2019**, *18*, 1026.
[7] K. N. Amato, S. M. Gaytan, L. E. Murr, E. Martinez, P. W. Shindo, J. Hernandez, S. Collins, F. Medina, *Acta Mater.* **2012**, *60*, 2229.
[8] D. Zhang, W. Niu, X. Cao, Z. Liu, *Mater. Sci. Eng., A* **2015**, *644*, 32.
[9] E. Chlebus, K. Gruber, B. Kuźnicka, J. Kurzac, T. Kurzynowski, *Mater. Sci. Eng., A* **2015**, *639*, 647.
[10] W. M. Tucho, P. Cuvillier, A. Sjolyst-Kverneland, V. Hansen, *Mater. Sci. Eng., A* **2017**, *689*, 220.
[11] N. Nadammal, S. Cabeza, T. Mishurova, T. Thiede, A. Kromm, C. Seyfert, L. Farahbod, C. Haberland, J. A. Schneider, P. D. Portella, G. Bruno, *Mater. Des.* **2017**, *134*, 139.
[12] L. Thijs, M. L. Montero Sistiaga, R. Wauthle, Q. Xie, J.-P. Kruth, J. Van Humbeeck, *Acta Mater.* **2013**, *61*, 4657.
[13] S.-H. Sun, K. Hagihara, T. Nakano, *Mater. Des.* **2018**, *140*, 307.
[14] H. Y. Wan, Z. J. Zhou, C. P. Li, G. F. Chen, G. P. Zhang, *J. Mater. Sci. Technol.* **2018**, *34*, 1799.
[15] I. Serrano-Munoz, T. Mishurova, T. Thiede, M. Sprengel, A. Kromm, N. Nadammal, G. Nolze, R. Saliwan-Neumann, A. Evans, G. Bruno, *Sci. Rep.* **2020**, *10*, 14645.
[16] N. Nadammal, T. Mishurova, T. Fritsch, I. Serrano-Munoz, A. Kromm, C. Haberland, P. D. Portella, G. Bruno, *Addit. Manuf.* **2021**, *38*, 101792.
[17] H. L. Wei, J. Mazumder, T. DebRoy, *Sci. Rep.* **2015**, *5*, 16446.
[18] M. Gäumann, C. Bezençon, P. Canalis, W. Kurz, *Acta Mater.* **2001**, *49*, 1051.
[19] D. W. Brown, J. D. Bernardin, J. S. Carpenter, B. Clausen, D. Spernjak, J. M. Thompson, *Mater. Sci. Eng., A* **2016**, *678*, 291.
[20] M. M. Attallah, R. Jennings, X. Wang, L. N. Carter, *MRS Bull.* **2016**, *41*, 758.
[21] K. Kempen, B. Vrancken, S. Buls, L. Thijs, J. Van Humbeeck, J.-P. Kruth, *J. Manuf. Sci. Eng.* **2014**, *136*, 061026.
[22] P. Mercelis, J. Kruth, *Rapid Prototype J.* **2006**, *12*, 254.

[23] J.-P. Kruth, J. Deckers, E. Yasa, R. Wauthlé, *Proc. Inst. Mech. Eng., B* **2012**, *226*, 980.
[24] P. J. Withers, H. K. D. H. Bhadeshia, *Mater. Sci. Technol.* **2001**, *17*, 366.
[25] T. Thiede, S. Cabeza, T. Mishurova, N. Nadammal, A. Kromm, J. Bode, C. Haberland, G. Bruno, *Mater. Perform. Charact.* **2018**, *7*, 717.
[26] S. Goel, M. Neikter, J. Capek, E. Polatidis, M. H. Colliander, S. Joshi, R. Pederson, *Mater. Des.* **2020**, *195*, 109045.
[27] P. Pant, S. Proper, V. Luzin, S. Sjöström, K. Simonsson, J. Moverare, S. Hosseini, V. Pacheco, R. Peng, *Addit. Manuf.* **2020**, *36*, 101501.
[28] L. Parry, I. A. Ashcroft, R. D. Wildman, *Addit. Manuf.* **2016**, *12*, 1.
[29] Y. Liu, Y. Yang, D. Wang, *Int. J. Adv. Manuf. Technol.* **2016**, *87*, 647.
[30] J. Robinson, I. Ashton, P. Fox, E. Jones, C. Sutcliffe, *Addit. Manuf.* **2018**, *23*, 13.
[31] B. Cheng, S. Shrestha, K. Chou, *Addit. Manuf.* **2016**, *12*, 240.
[32] J. H. Robinson, I. R. T. Ashton, E. Jones, P. Fox, C. Sutcliffe, *Rapid Prototype J.* **2018**, *25*, 289.
[33] T. Mishurova, S. Cabeza, T. Thiede, N. Nadammal, A. Kromm, M. Klaus, C. Genzel, C. Haberland, G. Bruno, *Metall. Mater. Trans. A* **2018**, *49*, 3038.
[34] P. J. Withers, H. K. D. H. Bhadeshia, *Mater. Sci. Technol.* **2001**, *17*, 355.
[35] I. Serrano-Munoz, T. Fritsch, T. Mishurova, A. Trofimov, D. Apel, A. Ulbricht, A. Kromm, R. Hesse, A. Evans, G. Bruno, *J. Mater. Sci.* **2021**, *56*, 5845.
[36] J. Schröder, T. Mishurova, T. Fritsch, I. Serrano-Munoz, A. Evans, M. Sprengel, M. Klaus, C. Genzel, J. Schneider, G. Bruno, *Mater. Sci. Eng., A* **2021**, *805*, 140555.
[37] T. Q. Phan, M. Strantza, M. R. Hill, T. H. Gnaupel-Herold, J. Heigel, C. R. D'Elia, A. T. DeWald, B. Clausen, D. C. Pagan, J. Y. Peter Ko, D. W. Brown, L. E. Levine, *Integr. Mater. Manuf. Innov.* **2019**, *8*, 318.
[38] T. Mishurova, I. Serrano-Munoz, T. Fritsch, A. Ulbricht, M. Sprengel, A. Evans, A. Kromm, M. Madia, G. Bruno, *A Critical Discussion on the Diffraction-Based Experimental Determination of Residual Stress in AM Parts*, ASTM International, West Conshohocken, PA **2020**, pp. 122–138.
[39] A. Ulbricht, S. J. Altenburg, M. Sprengel, K. Sommer, G. Mohr, T. Fritsch, T. Mishurova, I. Serrano-Munoz, A. Evans, M. Hofmann, G. Bruno, *Metals* **2020**, *10*, 1234.
[40] D. Deng, R. L. Peng, H. Brodin, J. Moverare, *Mater. Sci. Eng., A* **2018**, *713*, 294.
[41] J. Schneider, B. Lund, M. Fullen, *Addit. Manuf.* **2018**, *21*, 248.
[42] N. Nadammal, A. Kromm, R. Saliwan-Neumann, L. Farahbod, C. Haberland, P. D. Portella, *JOM* **2017**, *70*, 343.
[43] R. Hielscher, H. Schaeben, *J. Appl. Crystallogr.* **2008**, *41*, 1024.
[44] U. Kocks, C. Tomé, H. Wenk, A. Beaudoin, H. Mecking, *Texture and Anisotropy: Preferred Orientations in Polycrystals and Their Effect on Materials Properties*, Cambridge University Press, Cambridge **2000**.
[45] E. Macherauch, *Z. Angew. Phys.* **1961**, *13*, 305.
[46] I. Noyan, J. Cohen, *Residual Stress: Measurement by Diffraction and Interpretation, Materials Research and Engineering*, Springer, New York **2013**.
[47] ISO21432:2019, Non-destructive testing - Standard test method for determining residual stresses by neutron diffraction, https://www.iso.org/standard/75266.htm (accessed: April 2021).
[48] D. Dye, H. J. Stone, R. C. Reed, *Curr. Opin. Solid State Mater. Sci.* **2001**, *5*, 31.
[49] DIN-EN-15305:2009-01, Non-destructive testing – Test method for residual stress analysis by X-ray diffraction, https://www.beuth.de/en/standard/din-en-15305/106937421 (accessed: April 2021).
[50] M. T. Huchings, P. Withers, T. M. Holden, T. Lorentzen, *Introduction to the Characterization of Residual Stress by Neutron Diffraction*, CRC Press, Taylor & Francis, Boca Raton, FL **2005**, pp. 149–202.
[51] M. Boin, R. C. Wimpory, *JLSRF* **2016**, *2*, A100.
[52] M. Hofmann, W. Gan, J. Rebelo-Kornmeier, *JLSRF* **2015**, *1*, A6.
[53] C. Randau, U. Garbe, H.-G. Brokmeier, *J. Appl. Crystallogr.* **2011**, *44*, 641.
[54] A. Bertram, R. Glüge, *Solid Mechanics: Theory, Modeling, and Problems*, Springer, Cham **2015**.
[55] C. Kumara, A. R. Balachandramurthi, S. Goel, F. Hanning, J. Moverare, *Materialia* **2020**, *13*, 100862.
[56] P. J. Withers, M. Preuss, A. Steuwer, J. W. L. Pang, *J. Appl. Crystallogr.* **2007**, *40*, 891.
[57] H. Mughrabi, *Philos. Mag.* **2006**, *86*, 4037.
[58] Z. Wang, E. Denlinger, P. Michaleris, A. D. Stoica, D. Ma, A. M. Beese, *Mater. Des.* **2017**, *113*, 169.
[59] R. Ganeriwala, M. Strantza, W. King, B. Clausen, T. Phan, L. Levine, D. Brown, N. Hodge, *Addit. Manuf.* **2019**, *27*, 489.